# Transient response of Southern Ocean ecosystems during Heinrich stadials

**Himadri Saini[1,2], Katrin J. Meissner[1,2], Karin Kvale[4], Laurie Menviel[1,3]**

[1]Climate Change Research Centre, University of New South Wales, Sydney, New South Wales, Australia
[2]The Australian Research Council Centre of Excellence for Climate Extremes, Sydney, New South Wales, Australia
[3]The Australian Centre for Excellence in Antarctic Science, University of Tasmania, Hobart, Tasmania 7001, Australia
[4]GNS Science, 1 Fairway Drive, Avalon 5010, PO Box 30368, Lower Hutt 5040, NZ

**Key Points:**

- Simulated marine ecosystems and $CO_2$ respond linearly to the combined impact of freshwater addition and reduced iron flux into the ocean.
- A maximum of 7 ppm increase in $CO_2$ is simulated due to the AMOC shutdown and weakened iron fertilisation under MIS 3 boundary conditions.
- Reduced aeolian iron flux in the Southern Ocean during Heinrich Stadials can lead up to 6 ppm rise in $CO_2$.

Corresponding author: Himadri Saini, himadri.saini@unsw.edu.au

**Abstract**

Antarctic ice core records suggest that atmospheric $CO_2$ increased by 15 to 20 ppm during Heinrich stadials (HS). These periods of abrupt $CO_2$ increase are associated with a significant weakening of the Atlantic meridional overturning circulation (AMOC), and a warming at high southern latitudes. As such, modelling studies have explored the link between changes in AMOC, high southern latitude climate and atmospheric $CO_2$. While proxy records suggest that the aeolian iron input to the Southern Ocean decreased significantly during HS, the potential impact on $CO_2$ of reduced iron input combined with oceanic circulation changes has not been studied in detail. Here, we quantify the respective and combined impacts of reduced iron fertilisation and AMOC weakening on $CO_2$ by performing numerical experiments with an Earth system model under boundary conditions representing 40,000 years before present (ka). Our study indicates that reduced iron input can contribute up to 6 ppm rise in $CO_2$ during an idealized Heinrich stadial. This is caused by a 5% reduction in nutrient utilisation in the Southern Ocean, leading to reduced export production and increased carbon outgassing from the Southern Ocean. An AMOC weakening under 40ka conditions and without changes in surface winds leads to a $\sim$0.5 ppm $CO_2$ increase. The combined impact of AMOC shutdown and weakened iron fertilisation is almost linear, leading to a total $CO_2$ increase of 7 ppm. Therefore, this study highlights the need of including changes in aeolian iron input when studying the processes leading to changes in atmospheric $CO_2$ concentration during HS.

## 1 Introduction

Paleoproxy records from Greenland ice cores have shown the occurrence of abrupt climate variability during the last glacial period (Johnsen et al., 1972; Dansgaard et al., 1982; Kindler et al., 2014). Such variability, referred to as Dansgaard-Oeschger (D/O) variability, is characterized by an abrupt rise in Greenland air temperatures on decadal timescales (D/O event), followed by a gradual cooling over hundreds or thousands of years to cold (stadial) stages (G. Bond et al., 1993; Dansgaard et al., 1993). About twenty-five such climatic oscillations have been recorded in Greenland ice cores (Kindler et al., 2014) out of which 14 D/O events occurred during Marine Isotope Stage 3 (MIS 3, 65-27 thousand years before present (ka BP hereafter)). D/O stadials are associated with layers of ice rafted debris in North Atlantic marine sediment cores, indicating iceberg discharges into the ocean from the surrounding ice sheets (Van Kreveld et al., 2000). Some stadials are characterised by especially thick layers of ice rafted debris originating from the Laurentide ice-sheet (Heinrich, 1988; W. Broecker et al., 1992; Elliot et al., 1998; Snoeckx et al., 1999; Grousset et al., 2000), and are referred to as Heinrich Events (HEs). The origin and timing of D/O variability is still debated (W. S. Broecker et al., 1990; W. S. Broecker, 1994; G. C. Bond & Lotti, 1995; Hodell et al., 2010; Marcott et al., 2011; Barker et al., 2015; Menviel et al., 2020).

Paleoproxy records and modelling studies have suggested that Henirich stadials (HS), stadials which contain a HE, were associated with a significant weakening of the AMOC (Menviel et al., 2020). Such an AMOC weakening would lead to a reduction in the northward heat transport in the Atlantic, therefore causing a significant cooling in the North Atlantic and Greenland region (Ganopolski & Rahmstorf, 2001; Meissner et al., 2002; Huber et al., 2006; Kageyama et al., 2010; Buizert et al., 2014; Kindler et al., 2014; Henry et al., 2016; Menviel et al., 2020). Due to the reduced northward oceanic heat transport in the Atlantic, the AMOC weakening would lead to a warming in the South Atlantic, and at high southern latitudes (Crowley, 1992; Stocker, 1998; Blunier & Brook, 2001; Seidov & Maslin, 2001; Stocker & Johnsen, 2003; Jouzel et al., 2007; Timmermann et al., 2010; Pedro et al., 2018).

Antarctic ice core records reveal that there was a rise in atmospheric $CO_2$ concentration during Heinrich stadials (HS) (Ahn & Brook, 2008, 2014; Parrenin et al., 2013;

Bereiter et al., 2015; T. K. Bauska et al., 2021). Observations also suggest that concurrent to each HS in the North Atlantic during MIS 3, there was an Antarctic warm event (also known as Antarctic Isotope Maxima, AIM) coinciding with the $CO_2$ increase (Buizert et al., 2015; T. K. Bauska et al., 2021). For example, during Heinrich stadial 4 (H4), which is associated with an intense ice rafted debris deposition in the North Atlantic (Hemming, 2004), the temperature in Greenland decreased by ∼5°C (Huber et al., 2006; Kindler et al., 2014), while Antarctic temperatures rose by 2-3°C (Jouzel et al., 2007), and global $CO_2$ concentration increased by 15 to 20 ppm (Ahn & Brook, 2014; Bereiter et al., 2015; T. Bauska et al., 2018) (Figure 1a-c).

A compilation of numerical studies by Gottschalk et al. (2019) suggests that simulated atmospheric $CO_2$ levels can vary between -7 to +14 ppm in response to an AMOC shutdown under interglacial boundary conditions, whereas under glacial boundary conditions, this range can vary between -5 to +6 ppm. Modelling studies have further suggested that the rise in $CO_2$ during HS was caused by a decrease in deep Pacific and Southern Ocean carbon resulting from stronger North Pacific Deep Water (NPDW) formation and enhanced Southern Ocean outgassing (Huiskamp & Meissner, 2012; Menviel et al., 2014, 2018). Enhanced Southern Ocean outgassing could result from stronger convection or enhanced wind-driven upwelling as also suggested from paleo-proxy ventilation records (Anderson et al., 2009; Skinner et al., 2020).

Marine sediment cores from the South Atlantic (Martínez-García et al., 2011) and the South Pacific (Lamy et al., 2014) as well as Antarctic ice cores (Fischer et al., 2010; Lambert et al., 2012) have highlighted millennial-scale fluctuations in the atmospheric dust flux deposition at high southern latitudes that are opposite to changes in atmospheric $CO_2$ levels (Figure 1d). The associated changes in aeolian iron input to the ocean have been suggested to impact $CO_2$ concentration by modulating Southern Ocean nutrient utilisation (Martin, 1990; Martínez-García et al., 2014). Foraminifera-bound $\delta^{15}N$ (FB-$\delta^{15}N$) records (Martínez-García et al., 2014; Studer et al., 2015) suggest that the greater iron supply can stimulate higher nutrient utilisation in the ocean, by liberating the iron limitation effect, and causing higher export production (EP).

Many modelling studies have assessed the impact of changes in iron input to the ocean on Southern Ocean EP and atmospheric $CO_2$ by performing sensitivity experiments under Last Glacial Maximum (Aumont et al., 2003; Bopp et al., 2003; Oka et al., 2011; Lambert et al., 2015; Muglia et al., 2017; Khatiwala et al., 2019; Yamamoto et al., 2019; Lambert et al., 2021; Saini et al., 2021) and pre-industrial (PI) (Aumont & Bopp, 2006; Tagliabue et al., 2009, 2014) boundary conditions. However, even though the link between aeolian iron input and Southern Ocean EP should also hold for millennial scale climate changes (Anderson et al., 2014), the response of marine ecosystems and ocean biogeochemistry to changes in iron dust flux during millennial-scale events of the last glacial period has not been simulated in detail. So far, only one experiment studied the impact of millennial-scale changes in dust flux on atmospheric $CO_2$ by forcing the Bern3D model with reconstructed dust deposition from DOME C ice core under PI boundary conditions (Parekh et al., 2008). They simulated the largest increase in atmospheric $CO_2$ (+9 ppm) during H4 as a response to the lowest reconstructed aeolian dust flux.

Alkenone based EP evidence from a marine sediment core east of New Zealand, indicates higher productivity during HS over the past 70,000 years in this region (Sachs & Anderson, 2005). This is in agreement with the higher amount of opal flux during HS obtained from four cores in the Antarctic zone (south of ∼60°S in the Pacific sector and south of ∼50°S in the Atlantic sector) (Anderson et al., 2009). However, recent studies (Anderson et al., 2014; Martínez-García et al., 2014) based on alkenone concentrations, opal and organic carbon fluxes measured in sub-Antarctic Atlantic sediment cores (close to ∼40°S), point towards a reduction in biological productivity during HS when the dust supply declined (Lambert et al., 2012). This is also in agreement with the records of higher deep ocean oxygenation during HS in the sub-Antarctic Atlantic (Gottschalk

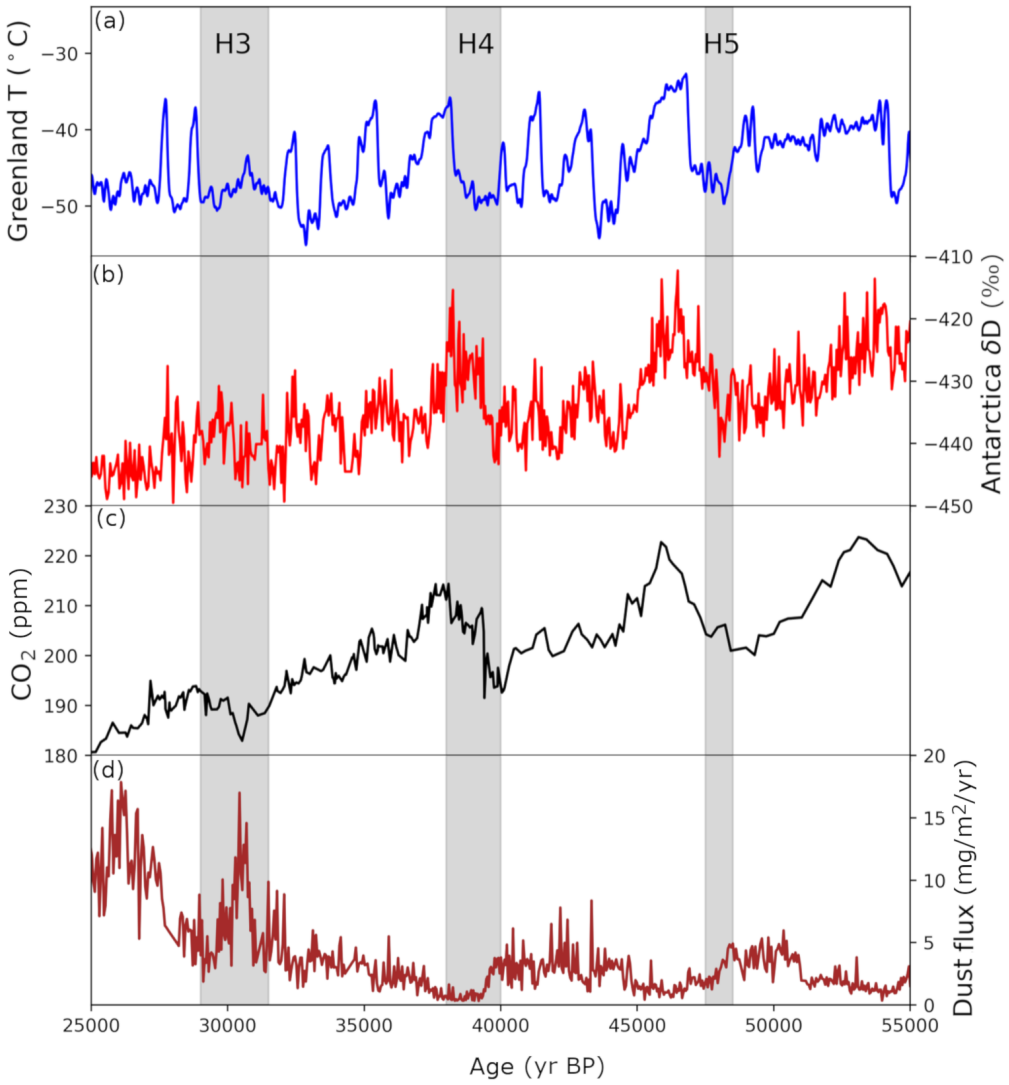


**Figure 1.** Time series of (a) Greenland air temperature anomalies compared to today (°C) reconstructed from the NGRIP ice core (Kindler et al., 2014); (b) Antarctic deuterium ($\delta$D) concentration (‰) anomaly from today as recorded in EPICA DOME C ice core (Jouzel et al., 2007), representing temperature variability in Antarctica; (c) atmospheric $CO_2$ concentrations (ppm) from EPICA DOME C ice core (Bereiter et al., 2015); (d) dust flux (mg/m$^2$/yr) from EPICA DOME C ice core (Lambert et al., 2012); Grey shade represents Heinrich stadials during MIS 3 (65-27 ka).

et al., 2016; Jaccard et al., 2016), which is an indicator of less remineralized organic carbon in the deep ocean. However, lower carbon sequestration in the ocean can also be due to increased ventilation as recorded from radiocarbon changes in the deep Southern Ocean during H4 (Gottschalk et al., 2016). Therefore, the Southern Ocean biological efficiency is impacted by more than just iron limitation. As there are only a few cores at sparse locations, it is thus challenging to draw robust conclusions about EP changes in the Southern Ocean during HS.

In addition, while many studies assessed the impact of an AMOC shutdown or an increase in aeolian iron input on the carbon cycle, no modelling study has yet looked into the combined impact of an AMOC shutdown and a decrease in aeolian iron flux on the carbon cycle under appropriate glacial boundary conditions. A study by Jochum et al. (2022) analysed the impact of longer stadials and reduced iron flux on global atmospheric $CO_2$ concentration. However, they investigated this response with an experiment resembling LGM climate conditions and iron flux reduced by 50% from PI dust flux. Here, we investigate the response of marine ecosystems and atmospheric $CO_2$ to the individual and combined impacts of AMOC shutdown and reduced iron flux input in the Southern Ocean under MIS 3 boundary conditions. We focus on the changes in ecosystems and atmosphere-ocean $CO_2$ exchange in the Southern Ocean as the iron fertilisation effect is crucial in this region (Saini et al., 2023).

## 2 Methods

### 2.1 Model

The experiments are performed with the version 2.9 University of Victoria Earth System Climate Model of intermediate complexity (UVic ESCM). It includes the MOM2 ocean general circulation model (Pacanowski, 1995) coupled to a sea ice model (Semtner, 1976; Hibler, 1979; Hunke & Dukowicz, 1997), a land surface scheme and a dynamic vegetation model (Meissner et al., 2003), a sediment model (Archer & Maier-Reimer, 1994; Meissner et al., 2012) with fixed weathering flux, and a vertically integrated 2-D energy and moisture balance atmospheric model (Fanning & Weaver, 1996). All model components are on a grid with a spatial resolution of 3.6 by 1.8 degrees and there are 19 vertical depth levels in the ocean. Seasonally varying solar insolation (Berger, 1978) at the top of the atmosphere and seasonal variations in wind stress and wind fields (Kalnay et al., 1996) are used as external forcing to drive the model. An ideal age tracer is added to track water mass age (Koeve et al., 2015). A detailed description of the model structure and physics can be obtained from (Weaver et al., 2001; Meissner et al., 2003; Eby et al., 2009; Mengis et al., 2020).

The climate model incorporates the recently developed ecosystem model called Kiel Marine Biogeochemistry Model (KMBM), v3 (Kvale et al., 2021; Saini et al., 2021), which represents the ocean carbon cycle. This model includes prognostic equations for diatoms (silicifying plankton) and coccolithophores (calcifying plankton), in addition to general phytoplankton and diazotrophs. It also includes a prognostic iron cycle (Nickelsen et al., 2015) featuring hydrothermal sources (Yao et al., 2019), and fully incorporated silica and $CaCO_3$ cycles. Full description of the ecosystem model can be found in Kvale et al. (2021).

### 2.2 Experimental design

A control simulation (40ka-control) using constant atmospheric $CO_2$ levels set at 200 ppm (Bereiter et al., 2015), with orbital forcing (Berger, 1978) and ice sheet topography (obtained from an offline ice sheet simulation (Abe-Ouchi et al., 2013)) corresponding to 40ka BP is integrated for 10,000 years to reach an equilibrium state. We use iron (LGM-fe) and silica (LGM-Si) dust fluxes based on the Last Glacial Maximum (LGM) dust deposition map from Lambert et al. (2012) and a iron/silica to dust percentage map

from Zhang et al. (2015), applying a 3% iron solubility factor in the ocean. After 10,000 years of spin up, the model is run with prognostic $CO_2$ for another 1,000 years (Figure 2, black line).

To simulate an idealized HS, we add a meltwater pulse of 0.05 Sv (equivalent to a 2 m global sea level rise) into the North Atlantic (52°W:5.4°E; 78°N:86°N) for 500 years (FW, Figure 2a, orange line, phase 1). This meltwater causes an AMOC shutdown. The model is run for another 500 years without any meltwater input (phase 2). To simulate an AMOC recovery, a salt flux addition to the North Atlantic is required in the UVic ESM. A negative meltwater input (-0.15 Sv) is thus added in the North Atlantic for 200 years. The model is then run for another 300 years (phase 3).

To understand the impact of reduced iron flux, we run another experiment called FE (Figure 2, red line), during which there is no freshwater forcing, but the global iron flux into the ocean is abruptly decreased by 90% to 2.744 Gmol $yr^{-1}$ (Figure 2g). This experimental design was chosen based on EPICA DOME C ice core records, where the optical particle counts as well as soluble calcium ($Ca^{2+}$) and non-sea salt soluble calcium ($nssCa^{2+}$) records indicate a reduction of dust flux by about 84% during H4, between 40ka and 38ka (Lambert et al., 2012). We run the model for 1000 years and then switch the iron flux back to the original LGM-fe flux value (27.44 Gmol $yr^{-1}$) in phase 3.

Finally, in our third experiment, FWFE (Figure 2, green line), we analyse the impact of the combination of a freshwater discharge into the North Atlantic and a simultaneous reduction in the iron input. Therefore, the iron flux is reduced by 90% and 0.05 Sv of meltwater is added in the North Atlantic during the first 500 years (phase 1). For the following 500 years, the iron flux stays reduced while no additional meltwater is added in the North Atlantic (phase 2). In phase 3, the salt is applied, the iron flux is changed back to the original value and the model is run for 200 years. After that the model continues to run for another 300 years with the same iron flux and no freshwater perturbation.

In each of these simulations, the North Atlantic Deep Water (NADW) transport is calculated as the maximum meridional Atlantic overturning streamfunction at 30°N between 1500 and 3500m depth. Antarctic Bottom Water transport (AABW) is calculated as the minimum meridional global overturning streamfunction at 35°S below 3000m depth. North Pacific Deep Water transport is calculated as the maximum meridional Indo-Pacific overturning streamfunction at 30°N below 700m depth.

In addition, simulated dissolved inorganic carbon (DIC) is decomposed into its three main contributors: respired organic carbon ($C_{reg}$), DIC generated by dissolution of calcium carbonate ($C_{CaCO_3}$) and preformed carbon ($C_{pref}$) following the methods described below.

### 2.3 $CO_2$ decomposition

Changes in sea surface $pCO_2$, which influence the magnitude and direction of air-sea flux exchange, are controlled by changes in sea surface temperature (SST), sea surface salinity (SSS), alkalinity (ALK) and DIC.

The sea surface $pCO_2$ anomalies can be decomposed into the individual contributions using the equations given below (Sarmiento & Gruber, 2006):

$$\Delta pCO_2 = \Delta pCO_2{}^{SST} + \Delta pCO_2{}^{SSS} + \Delta pCO_2{}^{ALK} + \Delta pCO_2{}^{DIC} \quad (1)$$

The SST contribution is derived from:

$$\Delta {pCO_2}^{SST} = e^{(\gamma_{SST} \times \Delta SST)} \times {pCO_2}^{ref} - {pCO_2}^{ref} \quad (2)$$

where $\gamma_{SST} = 0.0423$ (Sarmiento & Gruber, 2006), and ${pCO_2}^{ref}$ represents the sea surface $pCO_2$ value of the 40ka-control simulation.

Contributions from DIC, ALK, SSS are derived from:

$$\Delta {pCO_2}^{X} = \gamma_X \times \Delta X \times {pCO_2}^{ref} / \bar{X} \quad (3)$$

where, X represents DIC, ALK or SSS; $\bar{X}$ is the mean of X during PI; and $\gamma_X$ is equal to 13, -11 and 1 for DIC, ALK and SSS respectively (Sarmiento & Gruber, 2006; Smith & Marotzke, 2008; Egleston et al., 2010; Jiang et al., 2019).

# 3 Results

## 3.1 Carbon cycle response to an AMOC shutdown

As a response to the freshwater discharge in the North Atlantic in experiment FW (Figure 2a) during phase 1, the NADW transport decreases gradually from a maximum of ∼8 Sv and shuts off completely after 400 years of meltwater addition (Figure 2c) and until the end of phase 2. NPDW transport strengthens by ∼3 Sv over 1000 years, while AABW transport weakens initially by ∼1.5 Sv during phase 1 and then increases slightly during phase 2 (Figure 2d,e). Younger age of water masses at intermediate depths south of 30°S (Figure 2f, 3d-f) indicates enhanced Antarctic Intermediate water (AAIW) transport in the South Pacific by the end of phase 2.

As described elsewhere (Saenko et al., 2004; Okazaki et al., 2010), a weakening in NADW transport is accompanied by an enhanced NPDW formation in the North Pacific and AAIW formation in the Southern Ocean due to an increase in surface salinity arising from oceanic and atmospheric teleconnections with the North Atlantic (Figure 3b).

In agreement with earlier studies (Menviel et al., 2020), an inter-hemispheric thermal seesaw pattern, with a 3.3 degrees decrease in North Atlantic (35°W:10°W,47°N:55°N) sea surface temperatures (SSTs) and a 0.4 degrees increase in Southern Ocean SST, is simulated during the AMOC shutdown (Figure 3a). There is no significant change in the Southern Hemisphere annual mean sea ice edge, which is situated at 53°S in the Indian and Atlantic sectors and at 62°S in the Pacific sector (Figure 3a).

The combination of greater ocean stratification (attributable to higher SSTs and SSS), moderate increase in AAIW formation and the reduction in AABW transport lead to less surface nutrient availability during phase 1. Therefore, there is an overall decrease in both diatoms (by 3%) and coccolithophores (by 6%) abundance in the Southern Ocean during phase 1 (Figure 2h,j).

However, during phase 2, a further increase in AAIW formation, combined with a slow recovery of AABW leads to an increase in ventilation and deepening of the mixed layer depth (MLD) in the Southern Ocean (Figure 3c), which causes greater nutrient availability particularly in the Pacific sector. The locally increased nutrients are quickly taken up by the diatoms (being prescribed higher growth rates and half saturation constants for nutrients than coccolithophores (Kvale et al., 2021; Saini et al., 2021)), increasing diatom's abundance by ∼16% in the Pacific sector of the Southern Ocean, while coccolithophores decline (Figure 4a,b). This increase in diatoms is responsible for the total Southern Ocean diatom increase (+6.7%) shown in Figure 2h during phase 2. On the contrary, coccolithophores decrease by ∼9.6% in the Southern Ocean as they are outcompeted by diatoms (Figure 4b,2j). Overall, EP is 8.6% lower (Figure 2i,4c) and NPP 5% lower in the Southern Ocean (not shown) during the AMOC shutdown.

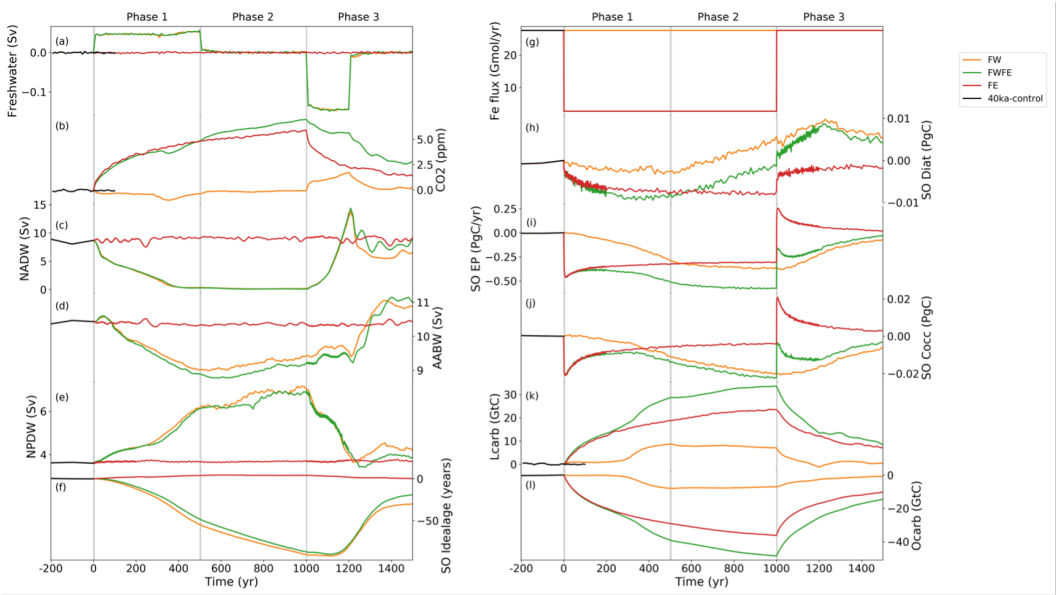


**Figure 2.** Transient evolution of simulated biological and physical variables. Time series of (a) freshwater flux (Sv) applied to the North Atlantic and (g) global iron flux (Gmol $yr^{-1}$), used as forcings in experiments (orange) FW, (red) FE, and (green) FWFE. Please note that the green line overlaps the orange line in (a) and the red line overlaps the green line in (g). The black line represents 200 years of 40ka-control experiment with prognostic $CO_2$. Time series of simulated (b) global atmospheric $CO_2$ concentration (ppm) anomaly compared to 40ka-control, (c) NADW (Sv), (d) AABW (Sv), and (e) NPDW transport (Sv), (f) Southern Ocean ideal age anomaly averaged over intermediate depths (600-1700m, years) compared to 40ka-control; time series anomalies of simulated (h) Southern Ocean depth integrated diatoms (PgC), (i) Southern Ocean export production at 177.5m depth (PgC), (j) Southern Ocean depth integrated coccolithophores (PgC), (k) global terrestrial carbon (GtC) and (l) global ocean carbon (GtC) compared to 40ka-control. The Southern Ocean (SO in the figure) is defined as the region south of 30°S, and all the biological tracers are integrated over the Southern Ocean.

**Table 1.** Changes in atmospheric $CO_2$, terrestrial and ocean carbon at the end of phase 2 (yr 1000) compared to the 40ka-control simulation.

| Experiments | Change in $CO_2$ (ppm) | Atmospheric carbon (GtC) | Terrestrial carbon (GtC) | Total Ocean carbon (GtC) | Atlantic, north of 30°S (GtC) | Pacific, north of 30°S (GtC) | Indian, north of 30°S (GtC) | Southern Ocean, south of 30°S (GtC) |
|---|---|---|---|---|---|---|---|---|
| FW | +0.5 | 1 | 7.5 | -8 | 140 | -120 | -19 | -9 |
| FE | +6 | 12 | 23 | -35 | 8 | 10 | -3 | -50 |
| FWFE | +7 | 14 | 31 | -45 | 145 | -110 | -21 | -59 |

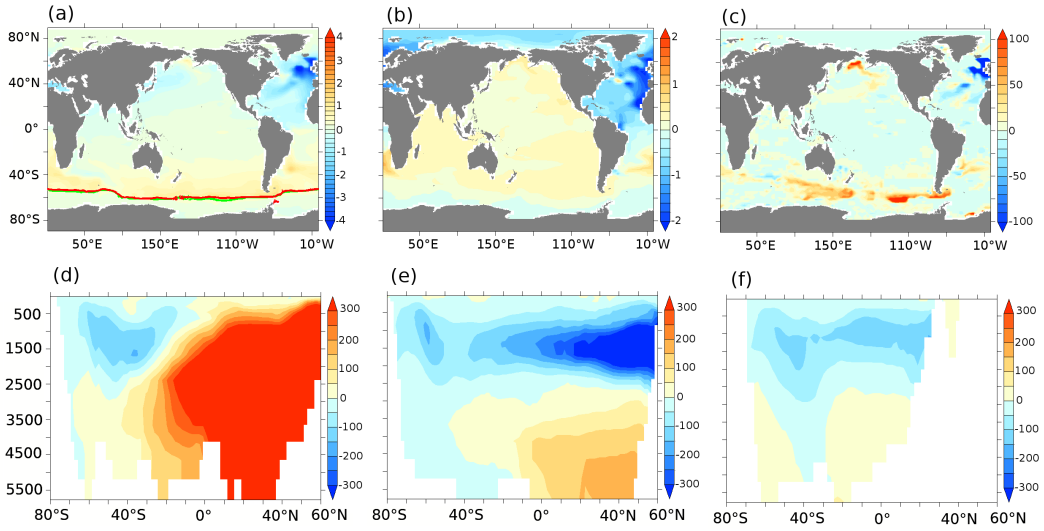


**Figure 3.** FW experiment at year 1000 (end of phase 2) minus 40ka-control anomalies of (a) sea surface temperature (°C), (b) sea surface salinity (psu), (c) ventilation depth (m), and zonally averaged ideal age (years) over the (d) Atlantic, (e) the Pacific, and (f) Indian sector; where red in d-f indicates reduction in ventilation. Overlaid contours in (a) represent the 15% annual mean sea-ice concentration in (red) 40ka-control and in (green) FW experiment at the end of phase 2.

In contrast, significantly weaker NADW transport and higher stratification, thus higher residence time, leads to a greater amount of regenerated phosphate ($P_{reg}$) at intermediate depths in the North Atlantic and in the deep Atlantic ocean (Figure S1). Correspondingly, DIC, in the form of regenerated carbon ($C_{reg}$) (Figure S2), accumulates in the Atlantic Ocean. Positive DIC anomalies are simulated below 500m depth in the North Atlantic and below 1500m depth in the South Atlantic (Figure 5a). At the end of phase 2, the Atlantic Ocean carbon reservoir has thus increased by 140 GtC (Table 1). On the contrary, the Pacific Ocean loses 120 GtC, because of increased ventilation associated with stronger NPDW and AAIW transports (Figure 2e,f, 3d-f, Table 1).

Enhanced intermediate depth ventilation in the Southern Ocean (Figure 2f), and to some extent lower Southern Ocean EP, leads to a decrease in DIC, and particularly in $C_{reg}$, in the upper 1000m of the Southern Ocean (Figure 5a-c, S2a-c). This anomaly spreads at intermediate depths within AAIW (Figure 5a-c). The positive DIC anomalies in the deep Pacific and Indian Ocean (Figure 5b,c) are mainly due to increased preformed carbon ($C_{pref}$) resulting from the lower nutrient utilisation at high southern latitudes (Figure S1, S2d-f). In the Indian Ocean, an increase in $C_{reg}$ is also simulated below 2500m depth (Figure S2c). Overall, DIC decreases by 19 GtC in the Indian Ocean and by 9 GtC in the Southern Ocean (Table 1, Figure 5c).

At the surface of the Southern Ocean, between ~47°S and 60°S, higher DIC concentration due to reduction in EP and higher ventilation, increases the surface ocean partial pressure of $CO_2$ ($pCO_2$, Figure 6b). Conversely, an increase in surface alkalinity in the Southern Ocean (Figure S3), associated with the decrease in coccolithophore population (Figure 4b), partly compensates the effect of higher DIC and ventilation on surface ocean $pCO_2$ (Figure 6b). In addition, higher SST and SSS lead to a reduction of $CO_2$ solubility in sea water (Figure 6b). Therefore, higher surface DIC and a weakened solubility pump cause a $CO_2$ outgassing in the Southern Ocean (red regions south of 30°S

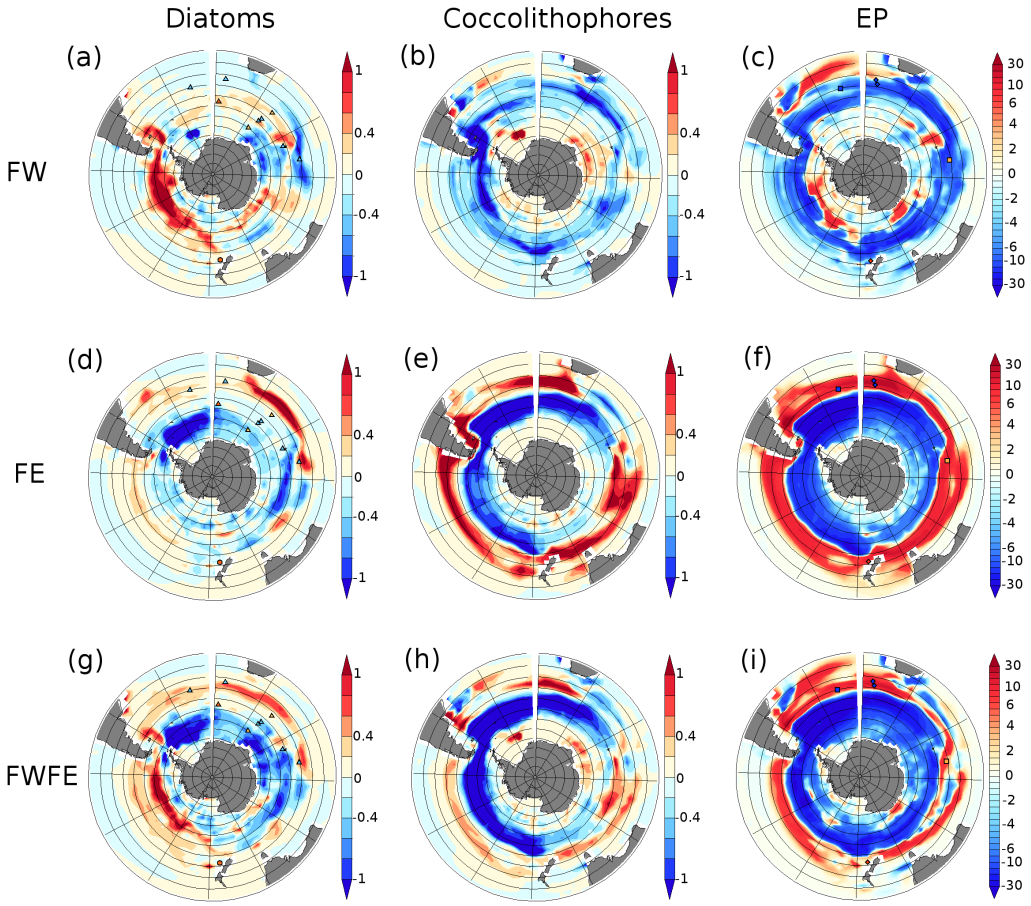


**Figure 4.** Diatoms, coccolithophores and EP anomalies for experiments (top) FW, (center) FE, and (bottom) FWFE at year 1000 (end of phase 2) compared to the 40ka-control simulation. Anomalies in depth integrated (a,d,g) diatoms (gC $m^{-2}$) and (b,e,h) coccolithophores (gC $m^{-2}$). (c,f,i) Export production anomalies at 177.5m (gC $m^{-2}yr^{-1}$). Paleo-proxy estimated anomalies at 39ka compared to 40ka are added on top of the simulated anomalies for qualitative comparison of model and data: (a, d, g) opal flux (triangles) (Anderson et al., 2009; Thöle et al., 2019; Amsler et al., 2022) and brassicasterol concentration (circle) (Sachs & Anderson, 2005); (c, f ,i) alkenone flux (diamonds) (Sachs & Anderson, 2003, 2005) and organic carbon flux (square) (Anderson et al., 2014; Thöle et al., 2019). Dark (light) orange represents significantly (slightly) higher values, while dark (light) blue represents significantly (slightly) lower values.

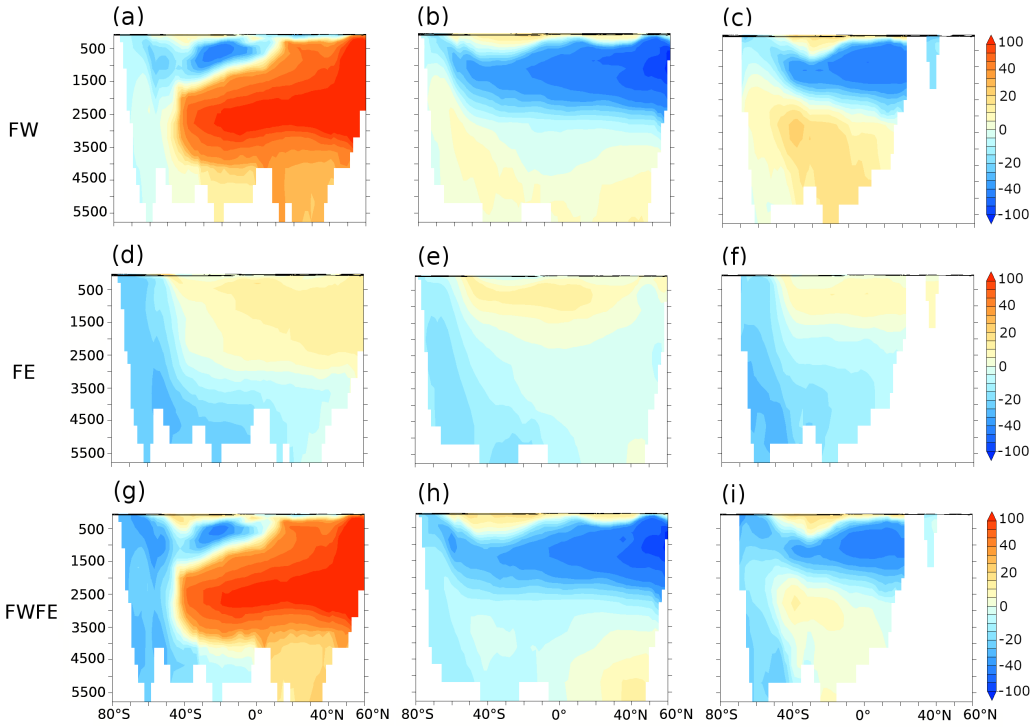


**Figure 5.** Zonally averaged DIC anomalies (mmol $m^{-3}$) over (left) the Atlantic, (center) the Pacific, and (right) Indian ocean for experiments (top) FW, (center) FE, and (bottom) FWFE at year 1000 (end of phase 2) compared to the 40ka-control simulation.

in Figure 7b), and particularly in the southeast Pacific between ∼47°S:60°S. In contrast, the increase in surface alkalinity leads to carbon drawdown from the atmosphere into the Southern Ocean (blue regions south of 40°S in Figure 7b). Overall, the Southern Ocean carbon outgassing decreases by ∼8%. We also see an anomalous outgassing from the north-east Atlantic (Figure 7b), which is due to a decrease in surface alkalinity (Figure 6a) in response to the freshwater flux addition in this region.

The changes in carbon exchange with the atmosphere causes the global ocean carbon to decrease by 8 GtC by the end of phase 2 (Table 1, Figure 2l). This is accompanied by a 7.5 GtC increase in terrestrial carbon reservoir (Figure 2k), and about 1 GtC carbon uptake by the atmosphere leading to an insignificant rise in $CO_2$ (Figure 2b) at the end of phase 2.

During the AMOC recovery in phase 3, the NADW transport increases to ∼14Sv before equilibrating at 7 Sv once the salt flux is turned off (Figure 2c). NPDW transport also reduces back to near initial conditions, while AABW transport stabilizes to a slightly higher value, at 11 Sv (Figure 2d,e). The addition of the salt flux causes a ∼1 ppm rise in $CO_2$, after which it reduces back to the initial value.

Diatoms increase by 21% compared to phase 2 in the Indian Ocean sector south of the annual sea ice edge, and coccolithophores increase by 6% mostly everywhere north of the annual sea ice edge (Figure S4a,b). This increases the total Southern Ocean EP by 7.6% at the end of phase 3 compared to phase 2 and brings EP back to a similar value as in 40ka-control.

### 3.2 Carbon cycle response to a reduction in aeolian iron flux.

When the aeolian iron input to the ocean is abruptly reduced (Figure 2g), the $CO_2$ increases by 6 ppm over 1000 years in experiment FE (Figure 2b). There are no changes in ocean circulation in this experiment, and therefore the changes in $CO_2$ are due to the reduction in the biological pump efficiency and the land carbon changes responding to higher $CO_2$ and temperatures. Plankton abundances south of ∼47°S are reduced due to decreased iron flux in the Southern Ocean (Figure 4d,e). Diatoms decrease by 19% in the Atlantic, 5.7% in the Pacific and ∼9.5% in the Indian sector south of ∼47°S, while coccolithophores decrease by 27% south of ∼47°S. This leads to reductions in EP (Figure 4f) and NPP south of ∼47°S.

Reduced nutrient utilization within the Antarctic zone causes an advection of excess nutrients northward (Figure S5), increasing diatoms (by 88% in the Indian region) and coccolithophores (by 23% in total) abundances and thus EP and NPP north of 47°S in the Southern Ocean (Figure 4d-f). Thereby, EP decreases by 17% south of 47°S and increases by 29% between 47°S and 30°S as a response to nutrient reorganization, with an overall 5.5% decrease in diatoms and 1.6% decrease in coccolithophores in the Southern Ocean. The total Southern Ocean EP decreases by 7% at the end of phase 2 (Figure 2i) due to a 5% decrease in nutrient utilisation in this sector.

The lower EP south of 47°S causes an increase in surface DIC. However, this also leads to reduced DIC, in the form of regenerated DIC ($C_{reg}$) within AABW (Figure 5d-f and S6a-c). These negative DIC anomalies are further advected into the deep Atlantic and Indo-Pacific basins (Figure 5d-f). In contrast, greater DIC content is simulated north of 47°S in the upper 2500m depth in all the basins. There is also a small increase in surface alkalinity in the Southern Ocean (Figure S3) due to the overall decrease in Southern Ocean coccolithophores (Figure 2j).

No significant changes in surface alkalinity, SST and SSS are simulated between 47°S and 60°S (Figure 6c). In contrast, higher surface DIC leads to ∼48% increase in $CO_2$ outgassing between 47°S and 60°S (Figure 6c and red regions south of 40°S in Figure 7c). This leads to a 50 GtC carbon loss from the Southern Ocean in experiment FE (Table 1). In total, while the global ocean loses 35 GtC (Figure 2l), the atmosphere gains 12 GtC, while 23 GtC are absorbed by the terrestrial biosphere (Figure 2k). During phase 3, $CO_2$ decreases gradually as the ocean biogeochemistry recovers to the initial conditions of 40ka-control.

### 3.3 Carbon cycle response to an AMOC shutdown and iron flux reduction

In this section we analyse the combined effect of an AMOC shutdown due to freshwater input in the North Atlantic (Figure 2a, experiment FWFE), and a reduced global iron flux (Figure 2g, experiment FWFE). A 7 ppm $CO_2$ increase is simulated in this experiment (1 ppm higher than FE and 6.5 ppm higher than FW).

As can be seen in Figure 2c-f, the changes in ocean circulation in FWFE are similar to those of the FW experiment, with slightly larger anomalies in AABW transport and slightly smaller anomalies in NPDW transport. Figures 2 and 4 clearly show that the diatom, coccolithophore and EP responses in FWFE experiment are a linear combination of the responses simulated in FW and FE.

Diatoms increase south of 47°S in the Pacific sector due to circulation changes as in experiment FW. However, because of the parallel reduction in iron supply (which causes 6% diatom reduction in this sector), the net increase is limited to 9.5% (instead of 16% as simulated in FW) compared to 40ka-control. Similarly, the diatoms decrease south of 47°S in the Atlantic (-16%, +3% from circulation and -19% from the iron effect) and

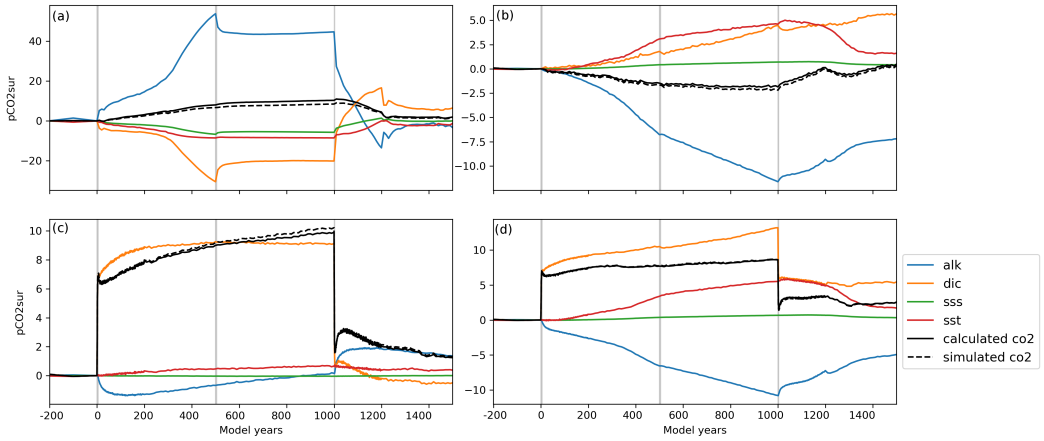


**Figure 6.** Time series of sea surface $pCO_2$ (ppm) anomalies resulting from changes in (blue) ALK, (orange) DIC, (green) SSS, and (red) SST for (a) FW averaged over the North Atlantic, (b) FW averaged over the Southern Ocean (47°S:60°S), (c) FE over the Southern Ocean (47°S:60°S), and (d) FWFE averaged over the Southern Ocean (47°S:60°S), compared to the 40ka-control simulation. The dashed black line represents simulated sea surface $pCO_2$ (ppm), while the solid black line shows the sum of the ALK, DIC, SSS and SST contributions. Please note the scale differs between the sub-panels.

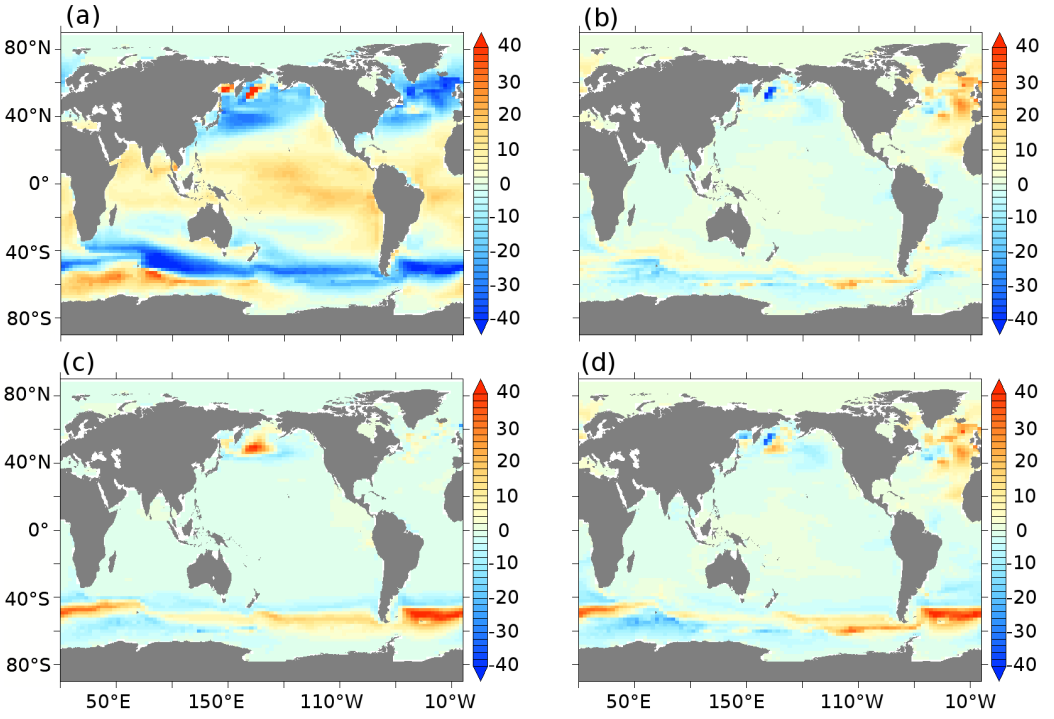


**Figure 7.** Surface carbon flux (gC $m^{-2}yr^{-1}$) for (a) 40ka-control; surface carbon flux anomalies for (b) FW, (c) FE, and (d) FWFE experiments at year 1000 (end of phase 2) compared to the 40ka-control simulation. Red indicates ocean outgassing.

Indian sectors (-14%, -3.2% from circulation and -9.5% from the iron effect) and the increase north of 47°S in the Indian sector (+63%) is also a net outcome from changes in both circulation and iron supply. Consequently, due to the weak positive anomalies in the Pacific, and the stronger negative anomalies in the Atlantic and Indian sectors, the Southern Ocean diatom abundance is 6% lower compared to FW but 5.8% higher compared to FE (Figure 2h) at the end of phase 2. Coccolithophores on the other hand decrease by 11.4% over the Southern Ocean (Figure 2j) compared to the 40ka-control (where 9.6% decrease is simulated due to the circulation changes as in FW and 1.6% is simulated due to changes in iron as in FE). With these changes in the plankton population, the total Southern Ocean EP reduces by 14% in FWFE at the end of phase 2 (Figure 4i).

The larger simulated decrease in $C_{reg}$ in the FWFE simulation (Figure S7a-c) compared to that in FW and FE, due to the weaker (-13%) Southern Ocean nutrient utilisation (Figure S8), causes a larger decrease in DIC below 200m depth in the Southern Ocean (Figure 5g-i). Simulated air-sea $CO_2$ fluxes in the FWFE experiment (Figures 6d and 7d) as well as the changes in ocean carbon (Table 1) in the Southern Ocean are a combination of FW and FE carbon changes. Therefore, a total of ∼45 GtC are lost from the ocean in experiment FWFE (Table 1, Figure 2l). Terrestrial carbon increases by 31 GtC (Figure 2k), while atmospheric carbon increases by 14 GtC by the end of phase 2.

## 4 Discussion

Our study indicates that to understand the mechanisms behind atmospheric $CO_2$ increase during HS, an investigation of dust related impacts is crucial in addition to previously explored feedbacks from oceanic circulation changes.

In our idealized experiment simulating a HS under MIS 3 boundary conditions, the simulated SST anomalies in the North Atlantic (∼-3°C) are consistent with the alkenone based SST proxies from the Iberian Margin (Martrat et al., 2007) and the North Atlantic (Cacho et al., 1999). On the contrary, the simulated Southern Ocean SST anomalies (+0.4°C) are significantly lower than what is inferred from marine records (+∼2°C) (Pahnke et al., 2003; Kaiser et al., 2005; Barker et al., 2009; Caniupán et al., 2011) but are still within the range of previously simulated responses to an AMOC shutdown (Kageyama et al., 2013; Menviel et al., 2014, 2015).

The changes in global circulation (Figure S9), and therefore the changes in Southern Ocean physics, impact marine ecosystems in this region. As pointed out earlier, high resolution paleo evidence of changes in EP during HS are limited. The simulated decrease in coccolithophores and EP at ∼45°S east of the South Island of New Zealand in our FW simulation (Figure 4b,c) is in contradiction with the increase in alkenone (proxy for EP) and $C_{37}$ methyl ketones (a marker for coccolithophores) concentrations recorded in a marine sediment core, MD97-2120 (Sachs & Anderson, 2005), at this location near Chatham Rise during H4 (Figure 4c). Our experiment FWFE, which includes the combined impact from the iron flux reduction (Figure 4e,f) and freshwater forcing (Figure 4b,c), improves this model data agreement by simulating an increase in coccolithophores and EP at this location (Figure 4h,i). The simulated increase in diatom abundance east of New Zealand, due to deeper MLD in experiments FW and FWFE, is in agreement with brassicasterol concentrations (a marker for diatoms) (Figure 4a,g) observed in the Chatham rise core (Sachs & Anderson, 2005). Increased diatom abundance south of ∼50°S in the Atlantic in FW and FWFE and a decrease in diatoms between ∼50°S and ∼55°S in the Indian sector in FE and FWFE, are also in agreement with the marine sediment opal flux records from the Southern Ocean (Anderson et al., 2009; Thöle et al., 2019; Amsler et al., 2022). In the sub-Antarctic, simulated diatom changes north of ∼50°S in FW are consistent with the proxy records from Atlantic (Sachs & Anderson, 2003; Anderson et al., 2014) and Indian sectors (Thöle et al., 2019; Amsler et al., 2022), while in the

FE and FWFE simulations, the diatom increase is consistent with only one record (Amsler et al., 2022) in the Indian sector.

The simulated EP increase at ∼45°S in simulations FE and FWFE is in contradiction with the reduced alkenone and organic carbon fluxes (Sachs & Anderson, 2003; Anderson et al., 2014) recorded in marine sediment cores in the subantarctic Atlantic. However, the simulated EP decrease south of 40°S in experiment FW is in agreement with these paleo EP records. The simulated increase in EP in the Indian sector is consistent with the organic carbon flux proxy (Thöle et al., 2019). In experiment FWFE, changes in the simulated diatom abundance and in EP show a ∼60% and 40% agreement with the available proxy records, respectively.

The simulated EP decrease in FW, along with the simulated decline south of ∼47°S in FE and FWFE experiments, is in agreement with the EP response to an AMOC shutdown obtained with another version of the UVic model (Menviel et al., 2014). Based on the above-mentioned proxy evidence and our simulated results, we suggest that an EP decrease due to reduced iron supply during HS could most likely have occurred south of ∼45°S in the Southern Ocean. Clearly, better constraints on changes in EP and plankton abundances during HS, along with additional proxy records of the last glacial millennial-scale climate variability are required.

Enhanced AAIW transport and reduction in Southern Ocean EP lead to an increase in intermediate and deep ocean oxygen concentrations south of ∼40°S in all of our simulations (Figure S10). This is in agreement with the reconstructed bottom water oxygen concentrations (Gottschalk et al., 2016), and authigenic Uranium based deep oxygenation records (Jaccard et al., 2016) in sub-Antarctic Atlantic marine sediment cores at ∼45°S and ∼55°S respectively.

A total of 7ppm $CO_2$ increase is simulated in experiment FWFE due to the compounding effects of changes in oceanic circulation and a reduced iron dust flux in the Southern Ocean. Most of this $CO_2$ increase is due to the reduced iron availability (experiment FE). This is caused by a larger carbon loss (50 GtC compared to 9 GtC) from the Southern Ocean in experiment FE compared to FW. In simulation FW, outgassing in the North Atlantic is compensated by the higher carbon sequestration (140 GtC in FW compared to 8 GtC in FE, Table 1) in the deep North Atlantic Ocean due to the AMOC shutdown, and by the decrease in outgassing in the Southern Ocean. Due to the $CO_2$ fertilization effect, the $CO_2$ increase in FWFE simulation enhances terrestrial primary productivity. This leads to a 12 GtC increase in terrestrial vegetation, as well as an increase in litter fall, leading to a 19 GtC increase in soil carbon. The total terrestrial carbon thus increases by ∼31 GtC. The simulated changes in terrestrial carbon in this study are in contradiction to previous modelling studies which show a decrease in terrestrial carbon in response to an AMOC shutdown (Scholze et al., 2003; Köhler et al., 2005; Menviel et al., 2008) but are in agreement with freshwater simulations performed with another version of the UVic ESCM (Huiskamp & Meissner, 2012). However, it should be noted that the discrepancies in these results could be related to having different vegetation models, different boundary conditions, and different freshwater flux forcings.

The 7 ppm rise is significantly lower than the maximum observed $CO_2$ increase of 20 ppm during HS within MIS 3 (Ahn & Brook, 2008; Bereiter et al., 2015; T. K. Bauska et al., 2021). It is also lower than the simulated increase of 9 ppm simulated by Parekh et al. (2008) as a response to reduced dust flux, although using a much simpler biogeochemical model than our study and under PI conditions. Jochum et al. (2022) simulated an increase of ∼8 ppm in $CO_2$ in their experiment with a longer stadial and a reduction in PI iron flux by 50%. The discrepancy between our simulated $CO_2$ changes and the estimates from proxy records can somewhat be explained by the lack of enhanced ventilation in the Southern Ocean in our simulations. Previous modelling studies have suggested that enhanced Southern Ocean ventilation could have contributed to the atmo-

spheric $CO_2$ increase (Menviel et al., 2014, 2015) during HS. Some of these changes in Southern Ocean ventilation changes could result from intensified Southern Hemisphere westerlies (Menviel et al., 2018; Huiskamp et al., 2016). In addition, recent studies have also highlighted the role of changes in AAIW in driving atmospheric $CO_2$ increases (Menviel et al., 2018; Yu et al., 2022). Due to the coarse resolution of the ocean model and lack of a dynamic atmosphere (and thus constant Southern Hemisphere westerlies) in the experiments presented above, it is possible that changes in Southern Ocean circulation and thus their impact on atmospheric $CO_2$ are not appropriately captured.

There is also uncertainty involving the total amount of dissolved iron available for uptake by phytoplankton under different climates. In the experiments presented here, we use 3% iron solubility, which is based on the most plausible estimate of glacial iron solubility (3-5%) (Conway et al., 2015; Shoenfelt et al., 2018; Saini et al., 2023). A higher iron solubility as initial MIS3 conditions would lead to greater $CO_2$ release when the iron supply is reduced (Saini et al., 2023). We also do not consider the impact of potential changes in ligand concentrations in the ocean which can also impact iron solubility (Parekh et al., 2006, 2008). Additionally, better constraints on the pattern and amount of dust fluxes under different climates are required to constrain the contribution of iron fertilisation during millennial events.

## Open Research Section

The modelling data from all the simulations are temporarily available at `https://datadryad.org/stash/share/sVMbSAD0s_UdVAIvhvE_psxF-I_RUts-W0ZtPjsOUr4` for the review process. The data will be published on the DRYAD repository through `https://doi.org/10.5061/dryad.k3j9kd5dt`, once the manuscript is accepted.


## Acknowledgments

Himadri Saini would like to acknowledge funding from the University International Postgraduate Award scheme at University of New South Wales. Model runs were undertaken with the assistance of resources from the National Computational Infrastructure (NCI), which is supported by the Australian Government. LM acknowledges funding from the Australian Research Council (ARC) grants FT180100606 and SR200100008. K.K. acknowledges support from the New Zealand Ministry of Business, Innovation and Employment within the Antarctic Science Platform, grant ANTA1801. K.K. also acknowledges support from the New Zealand Ministry of Business, Innovation and Employment (MBIE) through the Global Change through Time programme (Strategic Science Investment Fund, contract C05X1702). Katrin J. Meissner acknowledges funding from ARC DP180100048 and for computing through Merit Allocation Scheme and the UNSW HPC at NCI Scheme.


## References


Abe-Ouchi, A., Saito, F., Kawamura, K., Raymo, M. E., Okuno, J., Takahashi, K., & Blatter, H. (2013). Insolation-driven 100,000-year glacial cycles and hysteresis of ice-sheet volume. *Nature*, *500*(7461), 190–193.

Ahn, J., & Brook, E. J. (2008). Atmospheric co$_2$ and climate on millennial time scales during the last glacial period. *Science*, *322*(5898), 83–85.

Ahn, J., & Brook, E. J. (2014). Siple dome ice reveals two modes of millennial co$_2$ change during the last ice age. *Nature Communications*, *5*(1), 1–6.

Amsler, H. E., Thöle, L. M., Stimac, I., Geibert, W., Ikehara, M., Kuhn, G., ... Jaccard, S. L. (2022). Bottom water oxygenation changes in the southwestern indian ocean as an indicator for enhanced respired carbon storage since the last glacial inception. *Climate of the Past*, *18*(8), 1797–1813.

Anderson, R. F., Ali, S., Bradtmiller, L., Nielsen, S., Fleisher, M., Anderson, B., & Burckle, L. (2009). Wind-driven upwelling in the southern ocean and the deglacial rise in atmospheric $co_2$. *Science*, *323*(5920), 1443–1448.

Anderson, R. F., Barker, S., Fleisher, M., Gersonde, R., Goldstein, S. L., Kuhn, G., ... Sachs, J. P. (2014). Biological response to millennial variability of dust and nutrient supply in the subantarctic south atlantic ocean. *Philosophical Transactions of the Royal Society A: Mathematical, Physical and Engineering Sciences*, *372*(2019), 20130054.

Archer, D., & Maier-Reimer, E. (1994). Effect of deep-sea sedimentary calcite preservation on atmospheric $co_2$ concentration. *Nature*, *367*(6460), 260–263.

Aumont, O., & Bopp, L. (2006). Globalizing results from ocean in situ iron fertilization studies. *Global Biogeochemical Cycles*, *20*(2).

Aumont, O., Maier-Reimer, E., Blain, S., & Monfray, P. (2003). An ecosystem model of the global ocean including fe, si, p colimitations. *Global Biogeochemical Cycles*, *17*(2).

Barker, S., Chen, J., Gong, X., Jonkers, L., Knorr, G., & Thornalley, D. (2015). Icebergs not the trigger for north atlantic cold events. *Nature*, *520*(7547), 333–336.

Barker, S., Diz, P., Vautravers, M. J., Pike, J., Knorr, G., Hall, I. R., & Broecker, W. S. (2009). Interhemispheric atlantic seesaw response during the last deglaciation. *Nature*, *457*(7233), 1097–1102.

Bauska, T., Brook, E. J., Marcott, S., Baggenstos, D., Shackleton, S., Severinghaus, J., & Petrenko, V. (2018). Controls on millennial-scale atmospheric $co_2$ variability during the last glacial period. *Geophysical Research Letters*, *45*(15), 7731–7740.

Bauska, T. K., Marcott, S. A., & Brook, E. J. (2021). Abrupt changes in the global carbon cycle during the last glacial period. *Nature Geoscience*, *14*(2), 91–96.

Bereiter, B., Eggleston, S., Schmitt, J., Nehrbass-Ahles, C., Stocker, T. F., Fischer, H., ... Chappellaz, J. (2015). Revision of the epica dome c $co_2$ record from 800 to 600 kyr before present. *Geophysical Research Letters*, *42*(2), 542–549.

Berger, A. (1978). Long-term variations of daily insolation and quaternary climatic changes. *Journal of Atmospheric Sciences*, *35*(12), 2362–2367.

Blunier, T., & Brook, E. J. (2001). Timing of millennial-scale climate change in antarctica and greenland during the last glacial period. *Science*, *291*(5501), 109–112.

Bond, G., Broecker, W., Johnsen, S., McManus, J., Labeyrie, L., Jouzel, J., & Bonani, G. (1993). Correlations between climate records from north atlantic sediments and greenland ice. *Nature*, *365*(6442), 143–147.

Bond, G. C., & Lotti, R. (1995). Iceberg discharges into the north atlantic on millennial time scales during the last glaciation. *Science*, *267*(5200), 1005–1010.

Bopp, L., Kohfeld, K. E., Le Quéré, C., & Aumont, O. (2003). Dust impact on marine biota and atmospheric $co_2$ during glacial periods. *Paleoceanography*, *18*(2).

Broecker, W., Bond, G., Klas, M., Clark, E., & McManus, J. (1992). Origin of the northern atlantic's heinrich events. *Climate Dynamics*, *6*(3), 265–273.

Broecker, W. S. (1994). Massive iceberg discharges as triggers for global climate change. *Nature*, *372*(6505), 421–424.

Broecker, W. S., Bond, G., Klas, M., Bonani, G., & Wolfli, W. (1990). A salt oscillator in the glacial atlantic? 1. the concept. *Paleoceanography*, *5*(4), 469–477.

Buizert, C., Adrian, B., Ahn, J., Albert, M., Alley, R. B., Baggenstos, D., ... others (2015). Precise interpolar phasing of abrupt climate change during the last ice age. *Nature*, *520*(7549).

Buizert, C., Gkinis, V., Severinghaus, J. P., He, F., Lecavalier, B. S., Kindler, P., ... others (2014). Greenland temperature response to climate forcing during the last deglaciation. *Science*, *345*(6201), 1177–1180.

Cacho, I., Grimalt, J. O., Pelejero, C., Canals, M., Sierro, F. J., Flores, J. A., & Shackleton, N. (1999). Dansgaard-oeschger and heinrich event imprints in alboran sea paleotemperatures. *Paleoceanography*, *14*(6), 698–705.

Caniupán, M., Lamy, F., Lange, C., Kaiser, J., Arz, H., Kilian, R., ... others (2011). Millennial-scale sea surface temperature and patagonian ice sheet changes off southernmost chile (53 s) over the past 60 kyr. *Paleoceanography*, *26*(3).

Conway, T. M., Wolff, E. W., Röthlisberger, R., Mulvaney, R., & Elderfield, H. (2015). Constraints on soluble aerosol iron flux to the southern ocean at the last glacial maximum. *Nature communications*, *6*(1), 1–9.

Crowley, T. J. (1992). North atlantic deep water cools the southern hemisphere. *Paleoceanography*, *7*(4), 489–497.

Dansgaard, W., Clausen, H. B., Gundestrup, N., Hammer, C., Johnsen, S., Kristinsdottir, P., & Reeh, N. (1982). A new greenland deep ice core. *Science*, *218*(4579), 1273–1277.

Dansgaard, W., Johnsen, S. J., Clausen, H. B., Dahl-Jensen, D., Gundestrup, N., Hammer, C., ... others (1993). Evidence for general instability of past climate from a 250-kyr ice-core record. *Nature*, *364*(6434), 218–220.

Eby, M., Zickfeld, K., Montenegro, A., Archer, D., Meissner, K., & Weaver, A. J. (2009). Lifetime of anthropogenic climate change: Millennial time scales of potential $CO_2$ and surface temperature perturbations. *Journal of Climate*, *22*(10), 2501–2511. doi: 10.1175/2008JCLI2554.1

Egleston, E. S., Sabine, C. L., & Morel, F. M. (2010). Revelle revisited: Buffer factors that quantify the response of ocean chemistry to changes in dic and alkalinity. *Global Biogeochemical Cycles*, *24*(1).

Elliot, M., Labeyrie, L., Bond, G., Cortijo, E., Turon, J.-L., Tisnerat, N., & Duplessy, J.-C. (1998). Millennial-scale iceberg discharges in the irminger basin during the last glacial period: Relationship with the heinrich events and environmental settings. *Paleoceanography*, *13*(5), 433–446.

Fanning, A. F., & Weaver, A. J. (1996). An atmospheric energy-moisture balance model: Climatology, interpentadal climate change, and coupling to an ocean general circulation model. *Journal of Geophysical Research: Atmospheres*, *101*(D10), 15111–15128. Retrieved from `https://agupubs.onlinelibrary.wiley.com/doi/abs/10.1029/96JD01017` doi: 10.1029/96JD01017

Fischer, H., Schmitt, J., Lüthi, D., Stocker, T. F., Tschumi, T., Parekh, P., ... others (2010). The role of southern ocean processes in orbital and millennial $co_2$ variations–a synthesis. *Quaternary Science Reviews*, *29*(1-2), 193–205.

Ganopolski, A., & Rahmstorf, S. (2001). Rapid changes of glacial climate simulated in a coupled climate model. *Nature*, *409*(6817), 153–158.

Gottschalk, J., Battaglia, G., Fischer, H., Frölicher, T. L., Jaccard, S. L., Jeltsch-Thömmes, A., ... others (2019). Mechanisms of millennial-scale atmospheric $co_2$ change in numerical model simulations. *Quaternary science reviews*, *220*, 30–74.

Gottschalk, J., Skinner, L. C., Lippold, J., Vogel, H., Frank, N., Jaccard, S. L., & Waelbroeck, C. (2016). Biological and physical controls in the southern ocean on past millennial-scale atmospheric co 2 changes. *Nature communications*, *7*(1), 1–11.

Grousset, F. E., Pujol, C., Labeyrie, L., Auffret, G., & Boelaert, A. (2000). Were the north atlantic heinrich events triggered by the behavior of the european ice sheets? *Geology*, *28*(2), 123–126.

Heinrich, H. (1988). Origin and consequences of cyclic ice rafting in the northeast atlantic ocean during the past 130,000 years. *Quaternary research*, *29*(2), 142–152.

Hemming, S. R. (2004). Heinrich events: Massive late pleistocene detritus layers of the north atlantic and their global climate imprint. *Reviews of Geophysics*, *42*(1).

Henry, L., McManus, J., Curry, W., Roberts, N., Piotrowski, A., & Keigwin, L. (2016). North atlantic ocean circulation and abrupt climate change during the last glaciation. *Science*, *353*(6298), 470–474.

Hibler, W. D. (1979). *A Dynamic Thermodynamic Sea Ice Model* (Vol. 9) (No. 4). doi: 10.1175/1520-0485(1979)009⟨0815:adtsim⟩2.0.co;2

Hodell, D. A., Evans, H. F., Channell, J. E., & Curtis, J. H. (2010). Phase relationships of north atlantic ice-rafted debris and surface-deep climate proxies during the last glacial period. *Quaternary Science Reviews*, *29*(27-28), 3875–3886.

Huber, C., Leuenberger, M., Spahni, R., Flückiger, J., Schwander, J., Stocker, T. F., ... Jouzel, J. (2006). Isotope calibrated greenland temperature record over marine isotope stage 3 and its relation to ch4. *Earth and Planetary Science Letters*, *243*(3-4), 504–519.

Huiskamp, W., & Meissner, K. (2012). Oceanic carbon and water masses during the mystery interval: A model-data comparison study. *Paleoceanography*, *27*(4).

Huiskamp, W., Meissner, K., & d'Orgeville, M. (2016). Competition between ocean carbon pumps in simulations with varying southern hemisphere westerly wind forcing. *Climate Dynamics*, *46*(11-12), 3463–3480.

Hunke, E. C., & Dukowicz, J. K. (1997). An elastic-viscous-plastic model for sea ice dynamics. *Journal of Physical Oceanography*(Hibler 1979), 1849–1867. Retrieved from `http://journals.ametsoc.org/doi/pdf/10.1175/1520-0485(1997)027{\%}3C1849{\%}3AAEVPMF{\%}3E2.0.CO{\%}3B2`

Jaccard, S. L., Galbraith, E. D., Martínez-García, A., & Anderson, R. F. (2016). Covariation of deep southern ocean oxygenation and atmospheric co 2 through the last ice age. *Nature*, *530*(7589), 207–210.

Jiang, L.-Q., Carter, B. R., Feely, R. A., Lauvset, S. K., & Olsen, A. (2019). Surface ocean ph and buffer capacity: past, present and future. *Scientific Reports*, *9*(1), 1–11.

Jochum, M., Chase, Z., Nuterman, R., Pedro, J., Rasmussen, S., Vettoretti, G., & Zheng, P. (2022). Carbon fluxes during dansgaard–oeschger events as simulated by an earth system model. *Journal of Climate*, *35*(17), 5745–5758.

Johnsen, S. J., Dansgaard, W., Clausen, H., & Langway, C. (1972). Oxygen isotope profiles through the antarctic and greenland ice sheets. *Nature*, *235*(5339), 429–434.

Jouzel, J., Masson-Delmotte, V., Cattani, O., Dreyfus, G., Falourd, S., Hoffmann, G., ... others (2007). Orbital and millennial antarctic climate variability over the past 800,000 years. *Science*, *317*(5839), 793–796.

Kageyama, M., Merkel, U., Otto-Bliesner, B., Prange, M., Abe-Ouchi, A., Lohmann, G., ... others (2013). Climatic impacts of fresh water hosing under last glacial maximum conditions: a multi-model study. *Climate of the Past*, *9*(2), 935–953.

Kageyama, M., Paul, A., Roche, D. M., & Van Meerbeeck, C. J. (2010). Modelling glacial climatic millennial-scale variability related to changes in the atlantic meridional overturning circulation: a review. *Quaternary Science Reviews*, *29*(21-22), 2931–2956.

Kaiser, J., Lamy, F., & Hebbeln, D. (2005). A 70-kyr sea surface temperature record off southern chile (ocean drilling program site 1233). *Paleoceanography*, *20*(4).

Kalnay, E., Kanamitsu, M., Kistler, R., Collins, W., Deaven, D., Gandin, L., ... others (1996). The ncep/ncar 40-year reanalysis project. *Bulletin of the American meteorological Society*, *77*(3), 437–472.

Khatiwala, S., Schmittner, A., & Muglia, J. (2019). Air-sea disequilibrium enhances ocean carbon storage during glacial periods. *Science Advances*, *5*(6), eaaw4981.

Kindler, P., Guillevic, M., Baumgartner, M. F., Schwander, J., Landais, A., & Leuenberger, M. (2014). Temperature reconstruction from 10 to 120 kyr b2k from the ngrip ice core. *Climate of the Past*, *10*(2), 887–902.

Koeve, W., Wagner, H., Kähler, P., & Oschlies, A. (2015). 14 c-age tracers in global ocean circulation models. *Geoscientific Model Development*, *8*(7), 2079–2094.

Köhler, P., Joos, F., Gerber, S., & Knutti, R. (2005). Simulated changes in vegetation distribution, land carbon storage, and atmospheric co 2 in response to a collapse of the north atlantic thermohaline circulation. *Climate Dynamics*, *25*, 689–708.

Kvale, K., Keller, D. P., Koeve, W., Meissner, K. J., Somes, C. J., Yao, W., & Oschlies, A. (2021). Explicit silicate cycling in the kiel marine biogeochemistry model version 3 (kmbm3) embedded in the uvic escm version 2.9. *Geoscientific Model Development*, *14*(12), 7255–7285.

Lambert, F., Bigler, M., Steffensen, J. P., Hutterli, M., & Fischer, H. (2012). Centennial mineral dust variability in high-resolution ice core data from dome c, antarctica. *Climate of the Past*, *8*(2), 609–623.

Lambert, F., Opazo, N., Ridgwell, A., Winckler, G., Lamy, F., Shaffer, G., ... Abe-Ouchi, A. (2021). Regional patterns and temporal evolution of ocean iron fertilization and $co_2$ drawdown during the last glacial termination. *Earth and Planetary Science Letters*, *554*, 116675.

Lambert, F., Tagliabue, A., Shaffer, G., Lamy, F., Winckler, G., Farias, L., ... De Pol-Holz, R. (2015). Dust fluxes and iron fertilization in holocene and last glacial maximum climates. *Geophysical Research Letters*, *42*(14), 6014–6023.

Lamy, F., Gersonde, R., Winckler, G., Esper, O., Jaeschke, A., Kuhn, G., ... Kilian, R. (2014). Increased dust deposition in the pacific southern ocean during glacial periods. *Science*, *343*(6169), 403–407.

Marcott, S. A., Clark, P. U., Padman, L., Klinkhammer, G. P., Springer, S. R., Liu, Z., ... others (2011). Ice-shelf collapse from subsurface warming as a trigger for heinrich events. *Proceedings of the National Academy of Sciences*, *108*(33), 13415–13419.

Martin, J. H. (1990). Iron Hypothesis of $CO_2$ Change. *Paleoceanography*, *5*(1), 1–13.

Martínez-García, A., Rosell-Melé, A., Jaccard, S. L., Geibert, W., Sigman, D. M., & Haug, G. H. (2011). Southern ocean dust–climate coupling over the past four million years. *Nature*, *476*(7360), 312–315.

Martínez-García, A., Sigman, D. M., Ren, H., Anderson, R. F., Straub, M., Hodell, D. A., ... Haug, G. H. (2014). Iron fertilization of the subantarctic ocean during the last ice age. *Science*, *343*(6177), 1347–1350.

Martrat, B., Grimalt, J. O., Shackleton, N. J., de Abreu, L., Hutterli, M. A., & Stocker, T. F. (2007). Four climate cycles of recurring deep and surface water destabilizations on the iberian margin. *Science*, *317*(5837), 502–507.

Meissner, K., McNeil, B. I., Eby, M., & Wiebe, E. C. (2012). The importance of the terrestrial weathering feedback for multimillennial coral reef habitat recovery. *Global Biogeochemical Cycles*, *26*(3), 1–20. doi: 10.1029/2011GB004098

Meissner, K., Schmittner, A., Wiebe, E., & Weaver, A. (2002). Simulations of heinrich events in a coupled ocean-atmosphere-sea ice model. *Geophysical Research Letters*, *29*(14), 16–1.

Meissner, K., Weaver, A. J., Matthews, H. D., & Cox, P. M. (2003). The role of land surface dynamics in glacial inception: A study with the UVic Earth System Model. *Climate Dynamics*, *21*(7-8), 515–537. doi: 10.1007/s00382-003-0352-2

Mengis, N., Keller, D., MacDougall, A., Eby, M., Wright, N., Meissner, K., ... Zickfeld, K. (2020). Evaluation of the University of Victoria Earth System Climate Model version 2.10 (UVic ESCM 2.10). *Geoscientific Model Development, in press*.

Menviel, L., England, M. H., Meissner, K., Mouchet, A., & Yu, J. (2014). Atlantic-pacific seesaw and its role in outgassing $co_2$ during heinrich events. *Paleoceanography*, *29*(1), 58–70.

Menviel, L., Skinner, L. C., Tarasov, L., & Tzedakis, P. C. (2020). An ice–climate oscillatory framework for dansgaard–oeschger cycles. *Nature Reviews Earth & Environment*, *1*(12), 677–693.

Menviel, L., Spence, P., & England, M. H. (2015). Contribution of enhanced antarctic bottom water formation to antarctic warm events and millennial-scale atmospheric $co_2$ increase. *Earth and Planetary Science Letters*, *413*, 37–50.

Menviel, L., Spence, P., Yu, J., Chamberlain, M., Matear, R., Meissner, K., & England, M. H. (2018). Southern hemisphere westerlies as a driver of the early deglacial atmospheric $co_2$ rise. *Nature Communications*, *9*(1), 1–12.

Menviel, L., Timmermann, A., Mouchet, A., & Timm, O. (2008). Meridional reorganizations of marine and terrestrial productivity during heinrich events. *Paleoceanography*, *23*(1).

Muglia, J., Somes, C. J., Nickelsen, L., & Schmittner, A. (2017). Combined Effects of Atmospheric and Seafloor Iron Fluxes to the Glacial Ocean. *Paleoceanography*, *32*(11), 1204–1218. doi: 10.1002/2016PA003077

Nickelsen, L., Keller, D. P., & Oschlies, A. (2015). A dynamic marine iron cycle module coupled to the University of Victoria Earth System Model: The Kiel Marine Biogeochemical Model 2 for UVic 2.9. *Geoscientific Model Development*, *8*(5), 1357–1381. doi: 10.5194/gmd-8-1357-2015

Oka, A., Abe-Ouchi, A., Chikamoto, M. O., & Ide, T. (2011). Mechanisms controlling export production at the lgm: Effects of changes in oceanic physical fields and atmospheric dust deposition. *Global Biogeochemical Cycles*, *25*(2).

Okazaki, Y., Timmermann, A., Menviel, L., Harada, N., Abe-Ouchi, A., Chikamoto, M., ... Asahi, H. (2010). Deepwater formation in the north pacific during the last glacial termination. *Science*, *329*(5988), 200–204.

Pacanowski, R. (1995). Mom2 documentation user's guide and reference manual: Gfdl ocean group technical report. *Geophysical Fluid Dynamics Laboratory (GFDL), National Oceanic and Atmospheric Administration, Princeton, NJ*.

Pahnke, K., Zahn, R., Elderfield, H., & Schulz, M. (2003). 340,000-year centennial-scale marine record of southern hemisphere climatic oscillation. *Science*, *301*(5635), 948–952.

Parekh, P., Dutkiewicz, S., Follows, M., & Ito, T. (2006). Atmospheric carbon dioxide in a less dusty world. *Geophysical Research Letters*, *33*(3).

Parekh, P., Joos, F., & Müller, S. A. (2008). A modeling assessment of the interplay between aeolian iron fluxes and iron-binding ligands in controlling carbon dioxide fluctuations during antarctic warm events. *Paleoceanography*, *23*(4).

Parrenin, F., Masson-Delmotte, V., Köhler, P., Raynaud, D., Paillard, D., Schwander, J., ... Jouzel, J. (2013). Synchronous change of atmospheric $co_2$ and antarctic temperature during the last deglacial warming. *Science*, *339*(6123), 1060–1063.

Pedro, J. B., Jochum, M., Buizert, C., He, F., Barker, S., & Rasmussen, S. O. (2018). Beyond the bipolar seesaw: Toward a process understanding of interhemispheric coupling. *Quaternary Science Reviews*, *192*, 27–46.

Sachs, J. P., & Anderson, R. F. (2003). Fidelity of alkenone paleotemperatures in southern cape basin sediment drifts. *Paleoceanography*, *18*(4).

Sachs, J. P., & Anderson, R. F. (2005). Increased productivity in the subantarctic ocean during heinrich events. *Nature*, *434*(7037), 1118–1121.

Saenko, O. A., Schmittner, A., & Weaver, A. J. (2004). The atlantic–pacific seesaw. *Journal of Climate*, *17*(11), 2033–2038.

Saini, H., Kvale, K., Chase, Z., Kohfeld, K. E., Meissner, K. J., & Menviel, L. (2021). Southern ocean ecosystem response to last glacial maximum boundary conditions. *Paleoceanography and Paleoclimatology*, e2020PA004075.

Saini, H., Meissner, K. J., Menviel, L., & Kvale, K. (2023). Impact of iron fertilisation on atmospheric co 2 during the last glaciation. *Climate of the Past*, *19*(7), 1559–1584.

Sarmiento, J. L., & Gruber, N. (2006). *Ocean biogeochemical dynamics*. Princeton University Press.

Scholze, M., Knorr, W., & Heimann, M. (2003). Modelling terrestrial vegetation dynamics and carbon cycling for an abrupt climatic change event. *The Holocene*, *13*(3), 327–333.

Seidov, D., & Maslin, M. (2001). Atlantic ocean heat piracy and the bipolar climate see-saw during heinrich and dansgaard–oeschger events. *Journal of Quaternary Science: Published for the Quaternary Research Association*, *16*(4), 321–328.

Semtner, A. J. (1976). *A Model for the Thermodynamic Growth of Sea Ice in Numerical Investigations of Climate* (Vol. 6) (No. 3). doi: 10.1175/1520-0485(1976)006⟨0379:amfttg⟩2.0.co;2

Shoenfelt, E. M., Winckler, G., Lamy, F., Anderson, R. F., & Bostick, B. C. (2018). Highly bioavailable dust-borne iron delivered to the southern ocean during glacial periods. *Proceedings of the National Academy of Sciences*, *115*(44), 11180–11185.

Skinner, L., Menviel, L., Broadfield, L., Gottschalk, J., & Greaves, M. (2020). Southern ocean convection amplified past antarctic warming and atmospheric $co_2$ rise during heinrich stadial 4. *Communications Earth & Environment*, *1*(1), 1–8.

Smith, R. S., & Marotzke, J. (2008). Factors influencing anthropogenic carbon dioxide uptake in the north atlantic in models of the ocean carbon cycle. *Climate dynamics*, *31*(5), 599–613.

Snoeckx, H., Grousset, F., Revel, M., & Boelaert, A. (1999). European contribution of ice-rafted sand to heinrich layers h3 and h4. *Marine Geology*, *158*(1-4), 197–208.

Stocker, T. F. (1998). The seesaw effect. *Science*, *282*(5386), 61–62.

Stocker, T. F., & Johnsen, S. J. (2003). A minimum thermodynamic model for the bipolar seesaw. *Paleoceanography*, *18*(4).

Studer, A. S., Sigman, D. M., Martínez-García, A., Benz, V., Winckler, G., Kuhn, G., ... others (2015). Antarctic zone nutrient conditions during the last two glacial cycles. *Paleoceanography*, *30*(7), 845–862.

Tagliabue, A., Aumont, O., & Bopp, L. (2014). The impact of different external sources of iron on the global carbon cycle. *Geophysical Research Letters*, *41*(3), 920–926.

Tagliabue, A., Bopp, L., & Aumont, O. (2009). Evaluating the importance of atmospheric and sedimentary iron sources to southern ocean biogeochemistry. *Geophysical Research Letters*, *36*(13).

Thöle, L. M., Amsler, H. E., Moretti, S., Auderset, A., Gilgannon, J., Lippold, J., ... others (2019). Glacial-interglacial dust and export production records from the southern indian ocean. *Earth and planetary science letters*, *525*, 115716.

Timmermann, A., Menviel, L., Okumura, Y., Schilla, A., Merkel, U., Timm, O., ... Schulz, M. (2010). Towards a quantitative understanding of millennial-scale antarctic warming events. *Quaternary Science Reviews*, *29*(1-2), 74–85.

Van Kreveld, S., Sarnthein, M., Erlenkeuser, H., Grootes, P., Jung, S., Nadeau, M., ... Voelker, A. (2000). Potential links between surging ice sheets, circulation changes, and the dansgaard-oeschger cycles in the irminger sea, 60–18 kyr. *Paleoceanography*, *15*(4), 425–442.

Weaver, A. J., Eby, M., Wiebe, E. C., Bitz, C. M., Duffy, P. B., Ewen, T. L., ... Yoshimori, M. (2001). The UVic earth system climate model: Model description, climatology, and applications to past, present and future climates. *Atmosphere-Ocean*, *39*(4), 361–428. Retrieved from `http://www.tandfonline.com/doi/abs/10.1080/07055900.2001.9649686` doi: 10.1080/07055900.2001.9649686

Yamamoto, A., Abe-Ouchi, A., Ohgaito, R., Ito, A., & Oka, A. (2019). Glacial $CO_2$ decrease and deep-water deoxygenation by iron fertilization from glaciogenic

dust. *Climate of the Past*, *15*(3), 981–996.

Yao, W., Kvale, K. F., Achterberg, E., Koeve, W., & Oschlies, A. (2019). Hierarchy of calibrated global models reveals improved distributions and fluxes of biogeochemical tracers in models with explicit representation of iron. *Environmental Research Letters*, *14*(11), 114009.

Yu, J., Oppo, D. W., Jin, Z., Lacerra, M., Ji, X., Umling, N. E., ... others (2022). Millennial and centennial $co_2$ release from the southern ocean during the last deglaciation. *Nature Geoscience*, *15*(4), 293–299.

Zhang, Y., Mahowald, N., Scanza, R. A., Journet, E., Desboeufs, K., Albani, S., ... Fomba, K. W. (2015). Modeling the global emission, transport and deposition of trace elements associated with mineral dust. *Biogeosciences*, *12*(19), 5771–5792. doi: 10.5194/bg-12-5771-2015